

Spectrally Extended Line Field Optical Coherence Tomography Angiography

Si Chen

School of Electrical and Electronic Engineering, Nanyang Technological University, Singapore

Kan Lin

Nanyang Technological University

Linbo Liu (✉ LIULINBO@ntu.edu.sg)

Nanyang Technological University <https://orcid.org/0000-0001-6691-9253>

Article

Keywords:

Posted Date: December 16th, 2021

DOI: <https://doi.org/10.21203/rs.3.rs-1112611/v1>

License: © ⓘ This work is licensed under a Creative Commons Attribution 4.0 International License.

[Read Full License](#)

Abstract

The widespread usage of optical coherence tomography angiography (OCTA) is hindered by technical gaps including limited field of view (FOV), lack of quantitative flow information, and suboptimal motion correction. We introduce spectrally extended line field (SELF) OCTA that provides advanced solutions to these challenges. SELF-OCTA breaks the speed limitation and achieves two-fold gain in FOV without sacrificing microvascular details and signal strength through parallel imaging. It also relieves the requirement for shorter exposure time in wide-field applications, so that sufficient sensitivity to slow flow is maintained, particularly in spectral-domain OCT. Towards quantitative angiography, the 'frequency flow' mechanism overcomes the speed bottleneck by obviating the requirement for superfluous B-scans. In addition, this mechanism facilitates OCTA-data based motion tracking. Since it can be implemented in existing OCT devices without significant hardware modification or affecting existing functions, SELF-OCTA will make non-invasive, wide-field, quantitative, and low-cost angiographic imaging available to larger patient populations.

Introduction

Microvascular network imaging *in vivo* provides valuable insights into the understanding of a wide variety of diseases such as cardiovascular diseases, diabetes, neurodegenerative diseases, chronic kidney disease and cancers. In particular, microvascular impairment in retina has been biomarkers of not only blindness-threatening diseases such as diabetic retinopathy¹⁻⁶, but also disorders in other organs like brain and kidney and systemic diseases such as hypertension, providing a unique window to study the pathophysiology of the human microcirculation^{7,8}. Optical coherence tomography angiography (OCTA), a functional extension of OCT, is capable of highlighting blood flow signals noninvasively at the capillary level in three dimensions (3D) and obtains high-contrast angiograms quickly without the need for dye injection. Over the past decade, its use has been rapidly expanding in clinical practice and research, particularly with the commercialization of ophthalmic OCTA techniques in the past several years^{3-5,9-13}. However, the widespread usage of OCTA is still dependent on overcoming challenges such as limited field of view (FOV), motion artifacts, and lack of flow velocity quantification.

OCTA relies on moving red blood cells to contrast microvasculature against static tissue. This contrast signal induced by blood flow is extracted by detecting variations of OCT signals between consecutive B-scans taken at the same location. A typical OCT device adopt the point-scanning mechanism, in which the beam scanners steer the beam so that the light spot dwells at one lateral position at a time. Because of the sequential nature of this approach, achievable lateral FOV is solely dependent on A-line rate. This dependency is especially acute in angiographic imaging, since 2-5 repeated B-scans are required for motion contrast. In particular, spectral-domain OCT (SD-OCT) is limited in A-line rate as relative intensity noise (RIN) is inversely proportional to exposure time. As a result, FOV of most ophthalmic OCTA systems is much smaller than the standard-of-care technologies^{3,5}, even though capillary fine details are always sacrificed due to under-sampling^{5,14}. Swept-source technologies are promising in achieving ultra-wide

field OCTA with dramatically improved A-line rate, whereas, increases in imaging speed decrease the OCT signal and speed is ultimately limited by the signal to noise requirements given the constraint of allowable light exposure³. Therefore, the trade-off between FOV and signal quality is inherent with current OCTA, as long as both are solely dependent on the A-line rate.

Wide-field OCTA is not possible without effective tracking and correction of motion artifacts. For ophthalmic applications, eye tracking relies on additional imaging hardware such as infrared fundus camera or scanning laser ophthalmoscope¹⁵⁻¹⁷, which can extend the available imaging time beyond the few seconds when patients can fixate without saccades or blinking³. However, fundus images are not adequately sensitive to small motions due to their relatively low resolution. Since there is always a latency, there are errors that are not correctable by hardware-based eye tracking³. In addition, the increased system complexity and cost are also practical concerns. Self-navigated motion correction method represents a new trend to tackle these issues, which suppresses eye motion and blinking artifacts on wide-field OCTA without requiring any third-party hardware¹⁸. However, none of the existing software-based techniques is able to track lateral motion, leaving significant artifacts uncorrected. Improvement in motion artifact management requires a new technology that is capable of tracking motion with high precision and minimal latency, and ideally without additional hardware.

Quantification of flow velocity is of great interest with regards to disease diagnosis and management^{1-3, 5,19,20}. It has been well understood that OCTA flow signal is primarily affected by inter-scan time, which is the time interval between repeated B-scans at the same position. If the inter-scan time is long, the OCTA signal saturates easily for higher range of velocities, so that relation between flow speed and signal is nonlinear and complicated^{1,21-23}. In contrast, a short inter-scan time can better distinguish higher range of velocities; however, sensitivity to slow flow is reduced, as the red blood cells do not have sufficient time to move far enough to produce a detectable signal variance³. Choi¹⁹ and Wei²⁴ have managed to extend the dynamic range of detectable flow velocity by generating OCTA signals of multiple inter-scan time. However, these point-scanning based approaches requires more B-scan repeats than the standard OCTA, further limiting the FOV. A new technique capable of acquiring OCTA signals of multiple inter-scan time independent of the number of B-scan repeats is needed to have this important metric in routine applications.

The core of OCTA techniques is algorithms that computes OCT signal variations, which include, but not limited to, optical microangiography (OMAG)²⁵, speckle variance²⁶, phase variance²⁷, split-spectrum amplitude-decorrelation angiography (SSADA)²⁷ and correlation mapping²⁸. Interestingly, split-spectrum and subsequent frequency compounding increase the image quality for the algorithms most commonly implemented for ophthalmic applications^{29,30}. The reason is because speckle pattern is wavelength dependent, by splitting the full OCT spectrum into a number of narrower bands, frequency compounding reduces spectral-dependent speckle noise in flow-generated speckle signals³¹. The representative technique, SSADA, has been extensively validated in clinical settings^{1,2,6,19}. Splitting spectrum creates a new dimension for parallel image acquisition. Spectrally encoded OCT have been proposed to achieve

parallel structural image acquisition³². However, towards high-quality blood flow imaging, the frequency compounding method is not available.

We report a novel imaging platform, termed spectrally extended line field OCTA (SELF-OCTA), which achieves frequency-temporal compounding through a ‘frequency flow’ imaging mechanism. We demonstrate that SELF-OCTA provides advanced solutions to the above-mentioned challenges in human skin and retina *in vivo*.

Results

Line field and ‘frequency flow’ imaging mechanism

We have developed a 1300-nm SD-OCT system, which allows convenient switching between the SELF scheme and the standard point-scanning scheme (Fig. 1A). The construction of the 1300 nm SELF imaging system is mostly the same as a typical SD-OCT except that a set of prisms is introduced in the sample arm. The detection spectral bandwidth of the spectrometer is designed to be 152.3 nm centred at 1310 nm. With a collimating lens of 10 mm focal length and objective lens of 50 mm focal length, the theoretical lateral spot size at 1310 nm is $\sim 27 \mu\text{m}$ (full-width at half maximum, FWHM). The prisms spectrally extend the polychromatic beam to a line field along Y-axis in the focal plane of the objective lens (Fig. 1B). The line field length corresponding to the detected spectral bandwidth is estimated to be $\sim 278.6 \mu\text{m}$. Detailed information on system construction is provided in **Supplementary Information 1.1**.

Since the thermal damage threshold of an extended source is higher than the corresponding point source³³⁻³⁵, higher maximum permissible exposure (MPE) is allowed in favour of signal strength³⁶. By applying the ‘Most Restrictive Ratio’ method^{37,38}, the angular subtense in Y-axis generated by the prisms is $\sim 3.176 \text{ mrad}$ and the normalized partial power within the angular subtense is 0.799 (**Supplementary Fig. 1**). The corresponding wavelength range is approximately from 1251.9 nm to 1367.7 nm, covering a FOV of $159 \mu\text{m}$ in Y-axis (**Supplementary Fig. 1A**). Given an optical power incident on the skin of 4.74mW in the point-scanning scheme, the corresponding corrected power is 9.25 mW in the SELF scheme. Detailed method to determine the corrected sample power is provided in **Supplementary Information 1.2**.

The X-axis (fast axis) scanning protocol is identical between both schemes: the scanning step size Δx is set to be $12.8 \mu\text{m}$ to satisfy the Nyquist sampling requirement, and the number of repeated B-scans at the same location N equals to 2. The Y-axis (slow axis) scanning protocol, however, may be different. For the ease of comparison, we define Y-scan positions as Y positions illuminated by the first spectral band during each Y-scan cycle (Figs. 1C&D). In the point-scanning scheme, the inter-scan distance, which is the distance between two adjacent Y-scan positions, is equal to the X-axis scanning step size Δx , that is, Y image positions are the same as Y-scan positions (Fig. 1C). We follow SSADA algorithm to process data acquired from skin with the point-scanning system²⁷, in which we split the source spectrum into $M = 16$ equally spaced bands in wavenumber domain using Hamming filters (**Supplementary Fig. 2A** and **Supplementary Information**), and all M partial-spectrum decorrelation frames are averaged to

obtain the OCTA signal at one Y image position. In SELF-OCTA, we also split the source spectrum into M equally spaced bands using the same Hamming filters. The spacing between adjacent bands is $\Delta y = \Delta x$, so that each spectral band samples a distinct Y image position (Fig. 1D and Fig. 2A). The positioning error caused by the nonlinear frequency-space relation is negligible (**Supplementary Fig. 3**). By setting the inter-scan distance to be $L \cdot \Delta x$ ($L = 2, 4, 8, \text{ or } 16$), achievable FOV is multiplied by a factor of L . In general, M spectral bands acquired at j -th Y-scan position illuminate M consecutive Y image positions: $(j-1) \cdot L+1, (j-1) \cdot L+2, \dots, (j-1) \cdot L+M$, respectively. In other words, M/L light beams of distinct spectral bands dwell at the same lateral image position sequentially in time during Y-axis scan. This is analogous to the flow production process, where a number of Y image positions are addressed in parallel, and frequency components at each image position is ‘assembled’ during a number of consecutive Y-scan cycles. We term this slow axis imaging mechanism ‘frequency flow’.

The split-spectrum data is processed to generate M partial-spectrum decorrelation frames through Discrete Fourier transform (DFT) and amplitude decorrelation, which is similar to SSADA²⁷ (Fig. 2A). In general, m -th ($m = 1, 2, \dots, M$) partial-spectrum decorrelation frames acquired at j -th Y-scan position are assigned with an index number of $M(j-1) + m \cdot M/L - \text{quotient}[(m-1)/L]$. By doing so, the final OCTA signal at i -th Y image position is the average of partial-spectrum decorrelation frames with index number from $(i-1) \cdot M/L + 1$ to $i \cdot M/L$. Figs. 1D&2B illustrate a scanning protocol with $L = 2$, and $N = 2$, where M partial-spectrum decorrelation frames generated from spectral interference data acquired in j -th Y-scan position contribute to OCTA signals of M consecutive Y image positions. For example, in Fig. 2B the final decorrelation frame at the Y image position of $i = 15$ is obtained by averaging 8 partial-spectrum decorrelation frames: 15th frame at 1st Y scan position, 13th frame at 2nd Y scan position, 11th frame at 3rd Y scan position, 9th frame at 4th Y scan position, 7th frame at 5th Y scan position, 5th frame at 6th Y scan position, 3rd frame at 7th Y scan position and 1st frame at 8th Y scan position.

The Hamming window length is ~ 39 nm (**Supplementary Figs. 2A**), so that the axial resolution is measured to be $28.5 \mu\text{m}$ in skin with the refractive index of 1.38 (Fig. 2C). We model the multiplication between interferometric spectral data and a Hamming filter as a convolution in Y-axis, that is, the polychromatic lateral point-spread function along Y-axis is the convolution between the monochromatic point-spread function (PSF) and the Hamming window (**Supplementary Figs. 2B&C**). The lateral resolution is characterized by use of the 10-90% width of an edge scan profile as well as imaging a resolution chart (Figs. 2D&E). The lateral PSF in Y-axis is broadened to 1.51 times of the monochromatic PSF due to the convolution in Y-axis, which agrees well with the model (**Supplementary Fig. 2C**). We use a one-dimensional deconvolution algorithm to restore the lateral resolution along Y-axis in the *en face* projections (Fig. 2B). The 10-90% edge width restored by deconvolution is comparable to that of monochromatic light (Fig. 2D), so that isotropic spatial resolution is achieved in SELF-OCTA, which are also corroborated by the *en face* images of resolution chart (Fig. 2E). After deconvolution (lower panel, Fig. 2E), group 4 element 5 with line width of $19.69 \mu\text{m}$ can be unequivocally resolved in both X and Y directions, and Y-axis resolution is comparable to that of X-axis, which is the point-scanning direction.

Details of Hamming filters, deconvolution, and OCT structural image processing are provided in ***Supplementary Information 1.1&1.4.***

Twofold gain in field of view

We compare FOV between two schemes under the same conditions: 512 A-lines per B-frame, 400 Y-scan positions, and a total acquisition time of 4.096 s (Fig. 3). The FOV achieved with the point-scanning scheme is 6.55 mm x 5.12 mm (Figs. 3E1-4). SELF-OCTA provides twice as large FOV when we double the inter-scan distance as illustrated in Fig. 1D (Figs. 3F1-4&G1-4). With the same display contrast, the image quality of SELF-OCTA is comparable to that of the point-scanning scheme. First, through one-to-one comparison the vascular microstructures are almost identical between the point-scanning and SELF-OCTA images, including the capillary loops (Figs. E2, F2&G2). The SELF-OCTA *en face* images are slightly less crispy before deconvolution because of the convolution effect mentioned above (Figs. 3F1-4). Nevertheless, this insignificant issue is corrected after deconvolution (Figs. 3G1-4). Secondly, the penetration depth is also comparable as can be seen in the *en face* images of deep vascular plexus (Figs. E4, F4&G4), and cross-sectional angiograms (Figs. 3B-D and ***Supplementary Fig. 4.*** Thirdly, the mean decorrelation, measured from one-to-one matched vascular areas (***Supplementary Fig. 5.***), are also comparable between the point-scanning OCTA (0.206 ± 0.006) and SELF-OCTA (0.204 ± 0.004) (Fig. 3H) (student's t-test, $p = 0.23$). The speckle contrast of *en face* SELF-OCTA images (0.439 ± 0.059) is close to that of the point scanning scheme (0.353 ± 0.036), although the number of partial-spectrum decorrelation frames to be averaged at each Y image position is half of that of the point-scanning scheme. We attribute this relatively low speckle contrast to the fact that the partial-spectrum decorrelation frames at a Y image position are acquired at different time.

There are always visible motion artifacts, appeared as thin bright and dark lines, in *en face* angiograms acquired with the point-scanning scheme (Figs. 3E1-4, Figs. 4A1-3, and ***Supplementary Figs. 7A.*** The corresponding SELF-OCTA images are almost free of such artifacts, because motion induced signal deviations are distributed into 16 Y image positions, substantially suppressing the contrast of motion artifacts (Figs. 3F1-4&G1-4, Figs. 4B1-3). This artifact suppression mechanism is analogous to a selective low-pass filter along Y direction, which does not affect the signal. In a separate experiment, we deliberately generated motion artifacts by removing the vertical hand rest before image acquisition. Corresponding motion artifacts in SELF-OCTA *en face* images appear as low-intensity variations in the background (***Supplementary Fig. 6, Fig. 7B&C*** and ***Supplementary Movie 1.***

High sensitivity to slow flow

SELF-OCTA allows tailoring exposure time and inter-scan time without affecting FOV or total acquisition time. To validate this, we firstly acquired a 3D dataset with the point-scanning scheme with a nominal FOV of 6.55 mm x 6.55 mm and a total acquisition time of 3.28 s. The inter-scan time was 6.4 ms with an A-line rate of 80,384 Hz and 512 A-line per B-frame (Figs. 4A1-4). In the SELF scheme, we set the inter-scan distance to be $4\Delta x$ and the A-line rate to be 22,000 Hz, so that we were able to achieve 3.65 times longer inter-scan time and the same nominal FOV within 2.98 s (Figs. 4B1-3). Obviously, the advantage of

longer inter-scan time is the significantly increased sensitivity to slow flow in small vessels and capillaries, which are largely invisible in the point-scanning OCTA images due to relatively shorter inter-scan time (Figs. 4A1-3, 4B1-3, 4D&4E). Notably, a practical advantage of longer integration time is ~10% larger X-scan duty cycle (Figs. 4A3&B3).

In addition, most SD-OCT devices are RIN and electrical noise limited at working A-line rate. In the current device, total SNR is measured to be 9.94 dB lower at 80,384 Hz than that at 22,000 Hz A-line rates (Fig. 4C), which can be approximately broken down to 5.84-dB drop in signal due to reduced exposure time and 4.1-dB drop in signal to RIN ratio (SNR_{RIN}). This SNR_{RIN} drop significantly elevates the noise background and overwhelms weak vessel signals from small vessels (Fig. 4A1-3&4D) compared with SELF-OCTA images (Fig. 4B1-3&4E).

Multiple inter-scan time

Towards flow velocity quantification with high dynamic range, we have developed a partial B-frame scanning protocol that realizes multiple inter-scan time without increasing the number of B-scan repeats based on the SELF-OCTA platform. We split each B-scan of 384 A-lines into a half B-scan of 192 odd points (odd scan) and a half B-scan of 192 even points (even scan), so that there are 4 half-B-scans in a Y-scan cycle when $N = 2$ (Fig. 5A). OCTA images with inter-scan time of $\Delta T = 7.68$ ms and $\Delta T/2 = 3.84$ ms respectively can be achieved by re-arranging the order of half B-scans (Fig. 5A). Owing to the 'frequency flow' imaging mechanism, this protocol does not introduce any artifact since at each Y imaging position there are equal number of partial-spectrum decorrelation frames with inter-scan time of ΔT and $\Delta T/2$. It is worth mentioning that this partial B-frame scanning protocol does not work for the point-scanning platform with $N = 2$ since the inter-scan time, and consequently OCTA signal at odd and even pixels will be different.

For demonstration purpose, we introduce a simplified model to reconstruct angiograms with high dynamic range (Fig. 5B). Briefly, we assume that, over the decorrelation signal range of $[\sigma, \overline{D_{max}} - \sigma]$, flow velocities and decorrelation signals are linearly related, where $\overline{D_{max}}$ is the mean saturation decorrelation and σ is the standard deviation of the saturation decorrelation. Based on this assumption, the ratio between decorrelation signals acquired with ΔT ($D_{\Delta T}$) and $\Delta T/2$ ($D_{\Delta T/2}$) is a constant, α . If we multiply decorrelation profile of $\Delta T/2$ with α , the new decorrelation profile, $\alpha * D_{\Delta T/2}$, has a higher saturation limit (Fig. 5B). The high dynamic range *en face* angiogram is reconstructed using both the angiogram acquired with ΔT and the angiogram corresponding to $\alpha * D_{\Delta T/2}$. Detailed process to generate the high dynamic range angiogram is provided in **Supplementary Information 1.6**. Since this simplified model is based on a number of assumptions and approximations, readers are referred to previous phantom studies for an accurate model²¹⁻²³. Nevertheless, this high dynamic range angiogram combines the merits of both inter-scan time (Figs. 5C-E): signals from small vessels with slow flow speed are retained which are otherwise invisible or silent in angiograms acquired with $\Delta T/2$ (orange dash-line boxes, Fig. 5 C&E); signals from

vessels with high flow velocities that are saturated in angiogram acquired with ΔT become approximately linearly related with the corresponding flow velocities (blue solid-line boxes, Fig. 5 D&E). The high dynamic range is also evident in the corresponding histograms (Fig. 5F).

Motion tracking and correction with OCTA data

To demonstrate motion tracking and correction, the subject deliberately moved the hand in the lateral directions during image acquisition. Since the piano wire attached with the skin blocks the light (Fig. 6A), in the *en face* angiograms the shadow appears bright due to high decorrelation of background noise (Figs. 6B, 6F&6G). There is a 14-pixel overlap in Y-axis between *en face* projections of 3D angiograms acquired in each two adjacent Y-scan cycles, as can be appreciated with the images of an air bubble in the refractive index matching gel (arrow, Fig. 6B). In a representative experiment, 2D lateral motions can be measured at the subpixel level throughout the whole FOV (Figs. 6C&D). The range of detected motion velocity was from 0-2.2 $\mu\text{m}/\text{ms}$ (Fig. 6E). The performance of motion correction can be evaluated by comparing *en face* angiograms before (Fig. 6F) and after motion correction (Fig. 6G). The distorted piano wire image is largely corrected, which validates motion tracking and correction in the X direction. With an oblique direction of the piano wire with respect to Y-axis, the performance in both directions is demonstrated in ***Supplementary figs. 8&9***.

Retinal imaging *in vivo*

To validate SELF-OCTA for ocular imaging, we developed an ophthalmic SD-OCT centered at 1060 nm that can operate with both point-scanning and SELF scheme (***Supplementary Fig. 11***). Details on construction and characterization of the ophthalmic SD-OCT system is provided in ***Supplementary Information 2***. With $M = 8$ and $L = 2$, SELF-OCTA captures the same capillary details as the point scanning scheme but with twice as large FOV within the same acquisition time (Fig. 7), which is consistent with the results obtained in skin. The overall image quality of SELF *en face* angiogram is better than that of the point-scanning scheme in that the intensity of motion artifacts are dampened as explained above. In addition, trajectories of slow ocular motion are readily extracted from OCTA data (***Supplementary Fig. 13***), which are used to correct image distortions caused by ocular drift (Fig. 7D) and some of the vessel disruptions by microsaccades (blue arrows, Figs. 7C&D). OCT structural data were acquired 4 time faster than OCTA data and may serve as the reference for motion correction (***Supplementary Information 2.4***). The *en face* angiogram after correction matches better with the *en face* projection of OCT structural data than the uncorrected (***Supplementary Fig. 14***), validating the effectiveness of this method.

Discussion

Unlike OCT structural imaging where cross-sectional viewing is preferred, OCTA is inherently three dimensional and typically displayed with *en face* projections. Therefore, 2D and 3D priority scanning mechanisms are superior to the conventional depth priority scanning mechanism in terms of imaging

speed^{32,39-41}. As a 2D priority scanning platform, SELF-OCTA enables simultaneous signal acquisition from parallel lateral locations. This parallelization makes volumetric signal acquisition faster compared with the point-scanning scheme running with the same A-line rate. In achieving larger FOV, an important feature of SELF-OCTA lies in that it has more sensitivity budget than the point-scanning scheme as higher MPE is allowed. In this study, we show a two-fold gain in FOV with no penalty in signal compared with the point-scanning scheme. Larger FOV can be readily achieved by increasing inter-scan distance independent of specifications of light source or signal detection hardware. Currently, ultrafast OCT systems are not clinically available, at least not to large patient populations. SELF-OCTA makes it possible for clinical OCTA devices to break their speed limit and achieve more than two times wider FOV or higher sampling density by simply adding one optical element in the sample arm. SELF-OCTA will fill the gap between OCTA and the standard-of-care tools in FOV, providing invaluable information about vascular changes that involve peripheral retinal regions.

Lack of flow velocity information in the current clinical systems is also associated with the imaging speed limitation as revealed by previous phantom studies²¹⁻²⁴. Because of the above-mentioned trade-off between flow-signal linearity and sensitivity to slow flow, a wide range of inter-scan time from tens of microseconds to a few milliseconds are needed in order to cover the full range of retinal capillary flow from 0.4-3.0 mm/s^{21,24}. Current ultrahigh speed research prototypes provide an inter-scan time range of 1.5-4.5 ms, which are only applicable to flow velocity of <0.6 mm/s^{21,24}. Even this modest dynamic range requires at least three B-scan repeats²⁴. Eventually, more B-scan repeats will be needed to extend the range to the higher flow speed, which will be at substantial cost of imaging speed, and consequently FOV. The 'frequency flow' mechanism offered by the SELF-OCTA realizes multiple inter-scan time independent of B-scan repetition number. This unique capability overcomes the imaging speed bottleneck for velocimetry over large FOV. More importantly, since the inter-scan time of each partial-spectrum OCTA frames can be adjusted independently over a wide range through the partial B-frame approach, the optimal trade-off between dynamic range and sensitivity of flow detection can be achieved. Therefore, SELF-OCTA will potentially overcome a wide variety of challenges where differentiation of flow velocity and degrees of flow impairment is of great clinically significance, for example, lack of flow velocity in flow index of large vessels for assessing optic disc perfusion¹ and difficulties in quantifying slow flow in microaneurysms⁴².

Currently, SD-OCT is the most widely used system, mainly due to the matured technology, excellent phase stability for functional imaging, and lower cost. In SD-OCT, elevated RIN at high A-line rate prohibits this well-established technology from high-speed applications, particular when compared with SS-OCT where RIN is largely suppressed by dual-balanced detection¹¹. As a result, the speed of most SD-OCT clinical devices is limited to 70k Hz in contrast to 100-400 kHz of SS-OCTA³. SELF-OCTA disassociates imaging speed with exposure time and inter-scan time, which overcomes this standing problem and will make SD-OCTA viable for wide-field applications.

In the 'frequency flow' imaging mechanism, line-fields of adjacent Y-scan positions are overlapped in Y-axis, which for the first time makes it possible to track lateral motion with OCTA data. Current self-navigation motion correction method can only provide an indicator that motion occurred, and lack of quantitative lateral motion trajectory information results in artifacts such as vessel interruptions and low sensitivity of ocular drift¹⁸. SELF-OCTA may complement the self-navigation method. The typical angular velocity of ocular drift during fixation is 1°/s, which corresponds to a translational retinal motion of 0.17 μm/ms if the radius of retina is 10 mm. Such slow motions are readily detected with SELF-OCTA as shown in Fig. 7 and Supplementary Fig. 13. When signal to noise ratio is acceptable, vessel interruption caused by microsaccades can also be corrected (Fig. 7C). Combination of SELF-OCTA and self-navigation motion correction method will potentially obviate the problems with hardware-based tracking systems.

The total spectral bandwidth determines the angular subtense, which further determines the MPE and the length of line field. The most restrictive scenario for SELF-OCTA is posterior segment imaging centred at 1060 nm, where the maximum usable bandwidth is no more than 100 nm due to water absorption. In our study, to meet the Nyquist sampling requirement and maintain isotropic spatial resolutions, the length of the line field on retina is limited to ~85 μm, which is not enough for tracking microsaccades in the slow axis (asterisk in Fig. 7D). This limitation may be mitigated by reducing the inter-scan time so that the displacement along the slow axis in each B-scan cycle is within the length of the line field.

Deconvolution works well in restoring lateral resolution in Y-axis. Because deconvolution is an intensity-based model, there have been concerns when phase information is involved in the 3D coherent image formation⁴³. Other concerns of using deconvolution in imaging scattering tissues are that the optical transfer function may not be accurate and that it is sensitive to speckle and noise⁴³. In SELF-OCTA, artifacts associated with deconvolution are unnoticeable due to the following facts. First, the convolution involves phase information only in the depth dimension. Second, the speckle contrast is substantially reduced by frequency-temporal compounding as speckles of partial-spectrum decorrelation frames are fully uncorrelated (Supplementary Fig. 10). Thirdly, the optical transfer function is accurate since convolution is done digitally.

In conclusion, SELF-OCTA platform facilitates multiple important technological advancements towards wide field, high definition, quantitative, and low-cost angiographic imaging. SELF-OCTA breaks the speed limitation without sacrificing sensitivity, so that wide field imaging will be realistic in devices with speed limitation, in particular, the widely used SD-OCT. SELF-OCT also overcomes the speed bottleneck of quantitative flow velocity imaging, making this important function available with little cost. Last but not the least, OCTA-data based motion tracking capability may potentially simplify the complexity and reduce the cost of OCTA devices. In principle, by simple modifications in the sample arm, all the existing devices, regardless of type and A-line rate, should acquire these advanced imaging capabilities without affecting existing functions. We expect that SELF-OCTA will help with the study of the health and disorders of the human microcirculation and also make wide field, quantitative OCTA an inexpensive technology, therefore, easily accessible to larger patient populations.

Methods

Skin image acquisition and processing

Using 1300 nm imaging system, we imaged skin vasculatures at the palm side of the proximal interphalangeal joint of the middle finger in healthy human subjects. This study was approved by the Institutional Review Board (IRB) of Nanyang Technological University (IRB-2016-10-015). For the experiments conducted with the point-scanning scheme, the optical power incident on the skin was 4.74 mW when the total image acquisition time is 4.096 s (Fig. 3 and **Supplementary Fig. 7**); 9.1 mW when the total image acquisition time is 3.26 s (Fig. 4). We used ~9.10 mW for all the experiments with the SELF scheme. The optical power incident on the skin is below American National Standards Institute (ANSI) exposure limit for skin safety.

Skin images were acquired at an A-line rate of 50,000 Hz and 512 A-lines per B-frame for both schemes unless otherwise specified. For side-by-side comparison, we imaged the same skin region by careful alignment using cross-sectional OCT previews, except for **Supplementary Figs. 6&7** where images were acquired from another subject. We used home-made vertical and horizontal hand rests to minimize motion. We manually segmented the cross-sectional angiograms into three layers according to image depth with respect to the top of capillary loops (Figs. 3A-D): the first layer is ~180 μm thick in tissue, which includes most of capillary loops; the second layer is also ~180 μm thick in tissue, that mainly depicts subpapillary plexus; the third layer is ~360 μm thick in tissue, which corresponds to the skin layer with deep vascular plexus. Detailed information on image acquisition and image format are provided in **Supplementary Information 1.3**.

To demonstrate motion tracking and correction, we acquired OCTA images from human skin using 1300 nm imaging system while deliberately moving hands along the lateral directions (Fig. 6). Before image acquisition, we immobilized a short segment of piano wire (F1-8265, Fiber Instrument Sales, Inc.) to the skin surface with the refractive index matching gel. The wire was aligned along Y-axis or oblique with respect to Y-axis so that it served as the reference for lateral motion (Fig. 6A). As mentioned above, a 3D OCTA dataset is acquired during each Y-scan cycle with the SELF-OCTA scheme, which allows us to track lateral motion using *en face* projects of these 3D angiograms. Since each *en face* projection is 512×16 pixels ($X \times Y$) in size, with $L = 2$ there is an overlap of 14 pixels along Y-axis between projects of adjacent Y-scan cycles (Fig. 6B). We measured lateral displacement between the overlap portions by 2D cross-correlation⁴⁴. Note that we excluded the piano wire image from the input of the motion tracking. Details of motion tracking and correction algorithms are provided in **Supplementary Information 1.7**.

Retina image acquisition and processing

Using 1060 nm ophthalmic imaging system, we imaged the posterior segment of eyes of healthy human subjects. This study was approved by the Institutional Review Board (IRB) of Nanyang Technological University (IRB-2019-05-050). For the experiments conducted with the point-scanning scheme, the total image acquisition time was 4.73 s and optical power incident on the cornea was 1.754 mW. For the

experiments with the SELF scheme, the total image acquisition time for OCTA data was 4.73 s, and the optical power on the cornea was 3.20 mW (**Supplementary Information 2.2**). For both cases, the optical power is below ANSI exposure limit for eye safety.

Retinal angiograms were acquired with 67,590 Hz A-line rates for both the point scanning and the SELF scheme with the same data size: 400 A-lines per B-frame, 400 Y-scan positions, and $N = 2$ repeated B-scans per Y-scan position. For images acquired with the point-scanning scheme, FOV is 3.44 x 3.44 mm. For images generated with SELF-OCTA, FOV is 3.44 x 6.88 mm (width x height). With an estimated lateral resolution of $\sim 16.3 \mu\text{m}$ at retina, the sampling density for both scheme is close to Nyquist sampling requirement. For retinal angiograms, we used complex signal based method similar to OMAG after the whole spectrum was split into $M = 8$ equally spaced bands in wavenumber domain. Due to phase errors caused by eye motion, OCT structural images reconstructed from OCTA data suffer from motion artifacts. Therefore, an additional 3D structural scan was performed to acquire high resolution structural images. The detailed information on image acquisition and processing are available in **Supplementary Information 2.3&2.4**.

Declarations

Acknowledgement

We acknowledge the funding support from the Singapore Ministry of Health's National Medical Research Council under its Open Fund Individual Research Grant (MOH-OFIRG19may-0009), and the Ministry of Education Singapore under its Academic Research Funding Tier 2 (MOE-T2EP30120-0001).

Author contributions

L.L. conceived the project. S.C. developed the imaging systems. K.L. and S.C. participated in software development. S.C. and L.L. performed image acquisition and data analysis. L.L. and S.C. wrote the manuscript. All authors edited the final version of the paper.

Competing Interests

The authors declare no competing interests.

Data Availability

The datasets generated during and/or analysed during the current study are available from the corresponding author on reasonable request.

References

1. Jia, Y., *et al.* Optical Coherence Tomography Angiography of Optic Disc Perfusion in Glaucoma. *Ophthalmology* **121**, 1322–1332 (2014).

2. Jia, Y., *et al.* Quantitative Optical Coherence Tomography Angiography of Choroidal Neovascularization in Age-Related Macular Degeneration. *Ophthalmology* **121**, 1435–1444 (2014).
3. Spaide, R.F., Fujimoto, J.G., Waheed, N.K., Sadda, S.R. & Staurenghi, G. Optical coherence tomography angiography. *Progress in Retinal and Eye Research* **64**, 1–55 (2018).
4. Borrelli, E., Sarraf, D., Freund, K.B. & Sadda, S.R. OCT angiography and evaluation of the choroid and choroidal vascular disorders. *Progress in Retinal and Eye Research* **67**, 30–55 (2018).
5. Gao, S.S., *et al.* Optical Coherence Tomography Angiography. *Investigative Ophthalmology & Visual Science* **57**, OCT27-OCT36 (2016).
6. Jia, Y., *et al.* Quantitative optical coherence tomography angiography of vascular abnormalities in the living human eye. *Proceedings of the National Academy of Sciences* **112**, E2395-E2402 (2015).
7. Cheung, C.Y.-I., Ikram, M.K., Sabanayagam, C. & Wong, T.Y. Retinal Microvasculature as a Model to Study the Manifestations of Hypertension. *Hypertension* **60**, 1094–1103 (2012).
8. Zhang, Y., Wang, Y., Shi, C., Shen, M. & Lu, F. Advances in retina imaging as potential biomarkers for early diagnosis of Alzheimer’s disease. *Translational Neurodegeneration* **10**, 6 (2021).
9. Kashani, A.H., *et al.* Optical coherence tomography angiography: A comprehensive review of current methods and clinical applications. *Prog Retin Eye Res* **60**, 66–100 (2017).
10. Kashani, A.H., *et al.* Optical coherence tomography angiography: A comprehensive review of current methods and clinical applications. *Progress in Retinal and Eye Research* **60**, 66–100 (2017).
11. Xu, J., Song, S., Men, S. & Wang, R.K. Long ranging swept-source optical coherence tomography-based angiography outperforms its spectral-domain counterpart in imaging human skin microcirculations. *Journal of Biomedical Optics* **22**, 116007 (2017).
12. Vakoc, B.J., *et al.* Three-dimensional microscopy of the tumor microenvironment in vivo using optical frequency domain imaging. *Nature medicine* **15**, 1219–1223 (2009).
13. Kaicheng Liang, Z.W., Osman O. Ahsen, Hsiang-Chieh Lee, Benjamin M. Potsaid, Vijaysekhar Jayaraman, Alex Cable, Hiroshi Mashimo, Xingde Li, and James G. Fujimoto. Cycloid scanning for wide field optical coherence tomography endomicroscopy and angiography in vivo. *Optica* **5**, 36–43 (2018).
14. Ho, J., Dans, K., You, Q., Nudleman, E.D. & Freeman, W.R. COMPARISON OF 3 MM × 3 MM VERSUS 6 MM × 6 MM OPTICAL COHERENCE TOMOGRAPHY ANGIOGRAPHY SCAN SIZES IN THE EVALUATION OF NON-PROLIFERATIVE DIABETIC RETINOPATHY. *RETINA* **39**(2019).
15. Ferguson, R.D., Hammer, D.X., Paunescu, L.A., Beaton, S. & Schuman, J.S. Tracking optical coherence tomography. *Opt. Lett.* **29**, 2139–2141 (2004).
16. Hammer, D.X., *et al.* Advanced scanning methods with tracking optical coherence tomography. *Opt. Express* **13**, 7937–7947 (2005).
17. Zhang, Q., *et al.* Wide-field imaging of retinal vasculature using optical coherence tomography-based microangiography provided by motion tracking. *Journal of Biomedical Optics* **20**, 066008 (2015).

18. Wei, X., Hormel, T.T., Guo, Y., Hwang, T.S. & Jia, Y. High-resolution wide-field OCT angiography with a self-navigation method to correct microsaccades and blinks. *Biomed. Opt. Express* **11**, 3234–3245 (2020).
19. Choi, W., *et al.* Ultrahigh-Speed, Swept-Source Optical Coherence Tomography Angiography in Nonexudative Age-Related Macular Degeneration with Geographic Atrophy. *Ophthalmology* **122**, 2532–2544 (2015).
20. Ploner, S.B., *et al.* TOWARD QUANTITATIVE OPTICAL COHERENCE TOMOGRAPHY ANGIOGRAPHY: Visualizing Blood Flow Speeds in Ocular Pathology Using Variable Interscan Time Analysis. *RETINA* **36**, S118-S126 (2016).
21. Tokayer, J., Jia, Y., Dhalla, A.-H. & Huang, D. Blood flow velocity quantification using split-spectrum amplitude-decorrelation angiography with optical coherence tomography. *Biomed. Opt. Express* **4**, 1909–1924 (2013).
22. Choi, W.J., *et al.* Characterizing relationship between optical microangiography signals and capillary flow using microfluidic channels. *Biomed. Opt. Express* **7**, 2709–2728 (2016).
23. Su, J., *et al.* Calibration of optical coherence tomography angiography with a microfluidic chip. *Journal of Biomedical Optics* **21**, 086015 (2016).
24. Xiang Wei, T.T.H., Shaohua Pi, Yukun Guo, Yifan Jian, and Yali Jia. High dynamic range optical coherence tomography angiography (HDR-OCTA). *Biomed. Opt. Express* **10**, 3560–3571 (2019).
25. An, L. & Wang, R.K. In vivo volumetric imaging of vascular perfusion within human retina and choroids with optical micro-angiography. *Opt. Express* **16**, 11438–11452 (2008).
26. Barton, J.K. & Stromski, S. Flow measurement without phase information in optical coherence tomography images. *Opt. Express* **13**, 5234–5239 (2005).
27. Yali Jia, O.T., Jason Tokayer, Benjamin Potsaid, Yimin Wang, Jonathan J. Liu, Martin F. Kraus, Hrebesh Subhash, James G. Fujimoto, Joachim Hornegger, and David Huang. Split-spectrum amplitude-decorrelation angiography with optical coherence tomography. *Opt. Express* **20**, 4710–4725 (2012).
28. Jonathan, E., Enfield, J. & Leahy, M.J. Correlation mapping method for generating microcirculation morphology from optical coherence tomography (OCT) intensity images. *Journal of Biophotonics* **4**, 583–587 (2011).
29. Gorczynska, I., Migacz, J.V., Zawadzki, R.J., Capps, A.G. & Werner, J.S. Comparison of amplitude-decorrelation, speckle-variance and phase-variance OCT angiography methods for imaging the human retina and choroid. *Biomed. Opt. Express* **7**, 911–942 (2016).
30. Harrison, T.A., *et al.* Corneal endothelial cells possess an elaborate multipolar shape to maximize the basolateral to apical membrane area. *Mol Vis* **22**, 31–39 (2016).
31. Zhang, A., Zhang, Q., Chen, C.-L. & Wang, R. Methods and algorithms for optical coherence tomography-based angiography: a review and comparison. *Journal of Biomedical Optics* **20**, 100901 (2015).
32. Yelin, D., *et al.* Spectral-domain spectrally-encoded endoscopy. *Opt. Express* **15**, 2432–2444 (2007).

33. Vos, J.J. A theory of retinal burns. *The bulletin of mathematical biophysics* **24**, 115–128 (1962).
34. Zuclich, J., *et al.* *Laser-induced retinal damage threshold as a function of retinal image size*, (SPIE, 1999).
35. Beatrice, E.S. & Frisch, G.D. Retinal Laser Damage Thresholds as a Function of Image Diameter. *Archives of Environmental Health: An International Journal* **27**, 322–326 (1973).
36. ANSI. American National Standard for safe use of lasers (ANSI136.1). *ANSI 136.1-2000* (2000).
37. International Electrotechnical Commission, Safety of laser products - Part 1: Equipment classification and requirements. *IEC 60825-1 Edition 2.2*.
38. Schulmeister, K., *et al.* *Retinal thermal laser damage thresholds for different beam profiles and scanned exposure*, (SPIE, 2008).
39. Fechtig, D.J., *et al.* Line-field parallel swept source MHz OCT for structural and functional retinal imaging. *Biomed. Opt. Express* **6**, 716–735 (2015).
40. Egidijus Auksorius, D.B., Piotr Wegrzyn, Bartosz L. Sikorski, Ieva Zickiene, Kamil Lizewski, Mounika Rapolu, Karolis Adomavicius, Slawomir Tomczewski, Maciej Wojtkowski. Spatio-Temporal Optical Coherence Tomography provides advanced imaging of the human retina and choroid. *arXiv:2107.10672* (2021).
41. Stremplewski, P., *et al.* In vivo volumetric imaging by crosstalk-free full-field OCT. *Optica* **6**, 608–617 (2019).
42. Parrulli, S., *et al.* Microaneurysms visualisation using five different optical coherence tomography angiography devices compared to fluorescein angiography. *British Journal of Ophthalmology* **105**, 526 (2021).
43. Liu, Y.-Z., South, F.A., Xu, Y., Carney, P.S. & Boppart, S.A. Computational optical coherence tomography [Invited]. *Biomed. Opt. Express* **8**, 1549–1574 (2017).
44. Guizar-Sicairos, M., Thurman, S.T. & Fienup, J.R. Efficient subpixel image registration algorithms. *Opt. Lett.* **33**, 156–158 (2008).

Figures

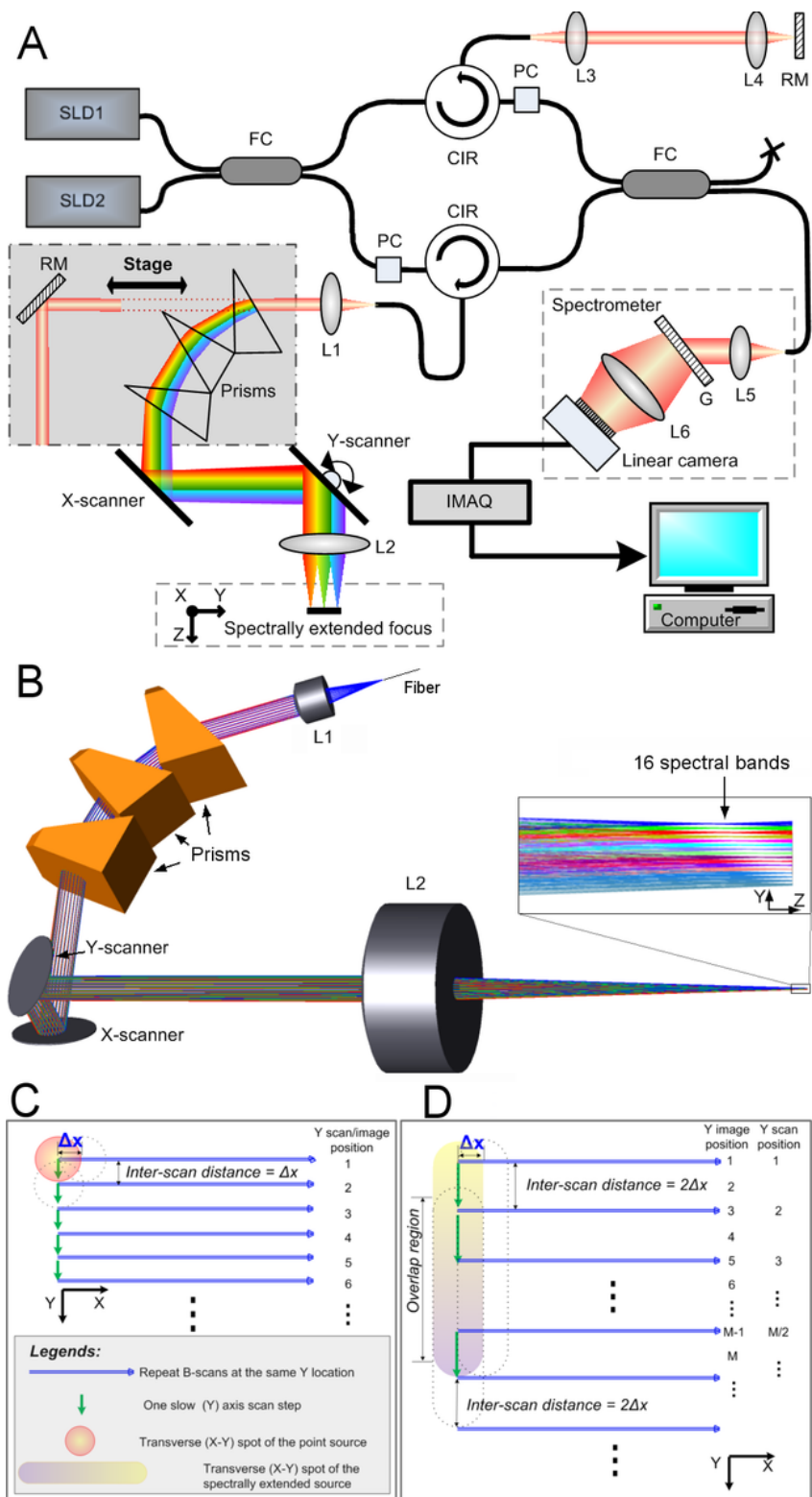


Figure 1

System construction and scanning protocol. (A) System schematic of SELF-OCTA. SLD1&SLD2: superluminescent diode sources; FC: fiber coupler; PC: polarization controller; CIR: circulator; L1-5: achromatic lenses; L6: camera lens; RM: reflective mirror; G: transmission grating; IMAQ: image acquisition card. (B) Three-dimensional layout of the sample arm optics and spectrally extended line field (inset). (C) Beam scanning protocol of the point-scanning scheme. Δx is the step size along the X-axis

and the inter-scan distance is the spacing between two consecutive Y-scan positions. Dashed circles represent spots of adjacent X/Y-scan positions, respectively. (D) Beam scanning protocol of SELF-OCTA. Dashed contours represent line fields of adjacent X/Y-scan positions, respectively. Note that the Y-scan position is the Y position illuminated by the first spectral band during each Y-scan cycle and is different from the Y image position.

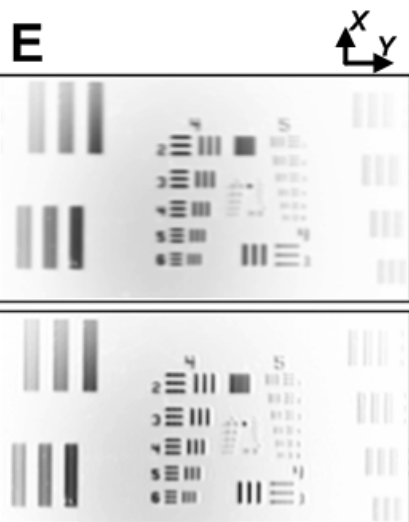
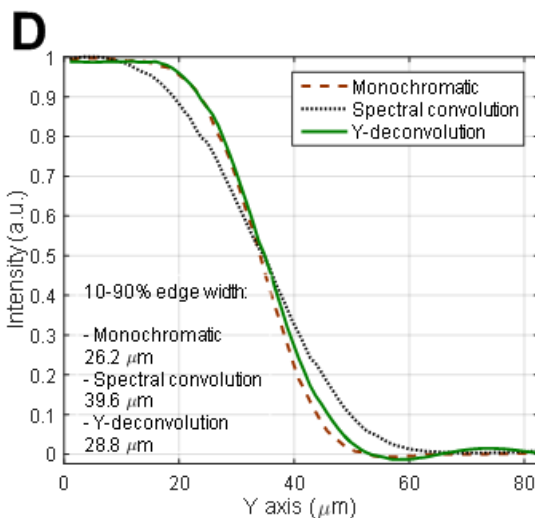
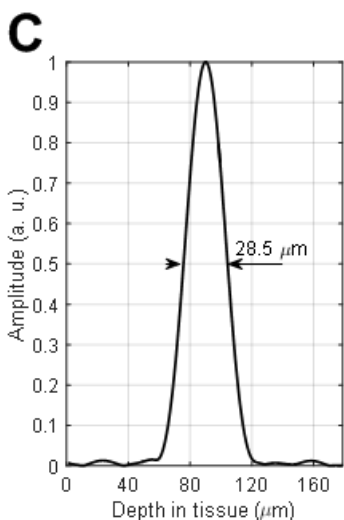
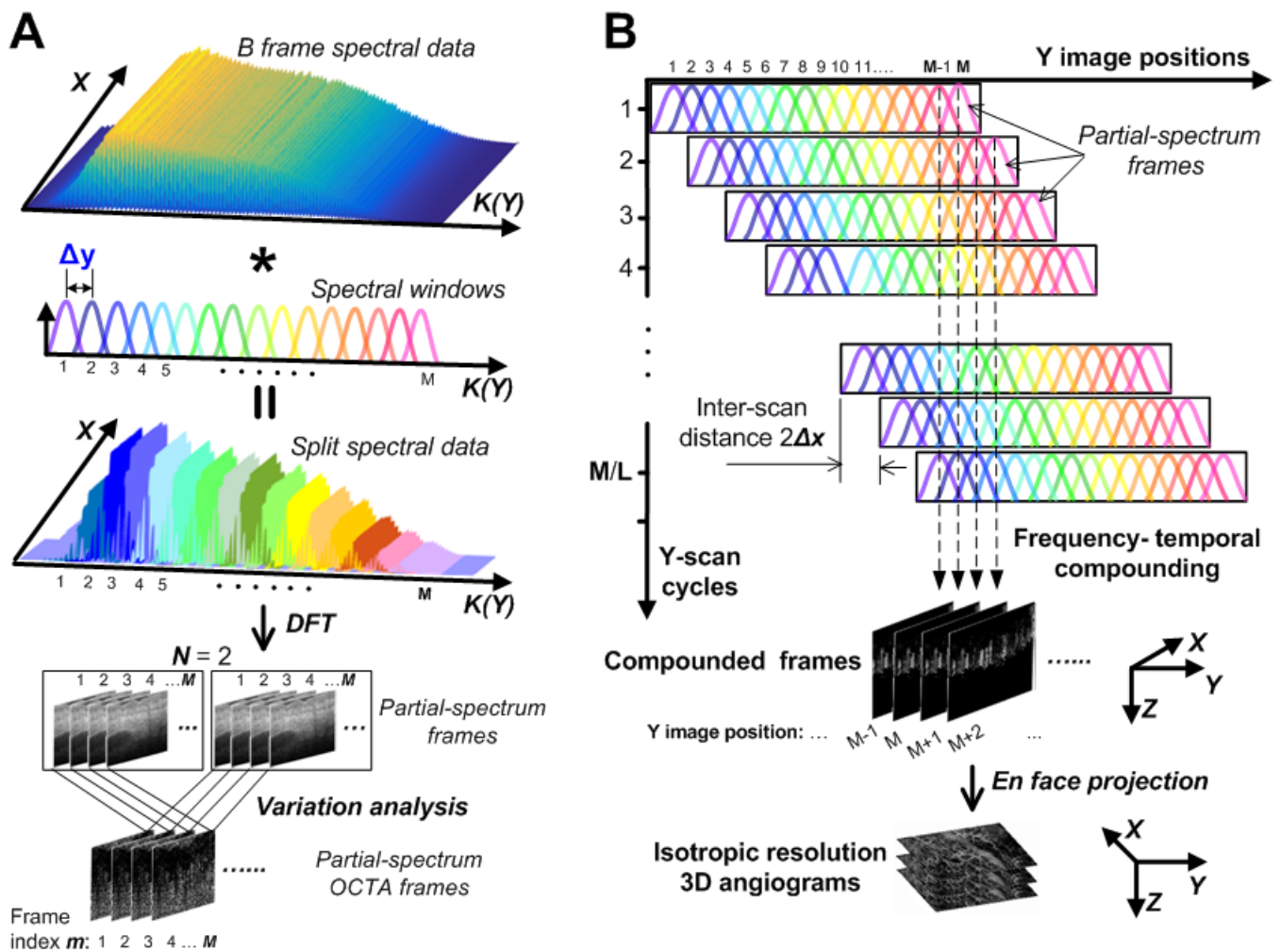


Figure 2

SELF-OCTA imaging mechanism and resolution characterization. (A) Process of spectrum splitting and OCTA signal analysis. K is the wavenumber and Δy is the spacing between Y image positions that equals to Δx . DFT: discrete Fourier transform. Spectral windows are hamming filters in this study. (B) “Frequency flow” imaging mechanism with $L = 2$. In the first Y-scan cycle, M spectral bands of the line field dwell at Y image positions of 1 to M , respectively. In each Y-scan cycle, the image position numbers covered by the line field increase by $L = 2$. For a given Y image position, the final OCTA signal (compounded frame) is the average of (M/L) partial-spectrum frames that are sequentially acquired from the Y image position. (C) OCT depth profile of a partial reflector as the sample. (D) 10-90% edge scan profiles of a monochromatic beam and the beam of the eighth spectral band (convolution in Y-axis). The green solid profile (Y-deconvolution) is obtained by deconvoluting the latter along Y-axis. (E) *En face* images of USAF 1951 resolution chart obtained using the beam of the eighth spectral band before (upper panel) and after Y-deconvolution (lower panel).

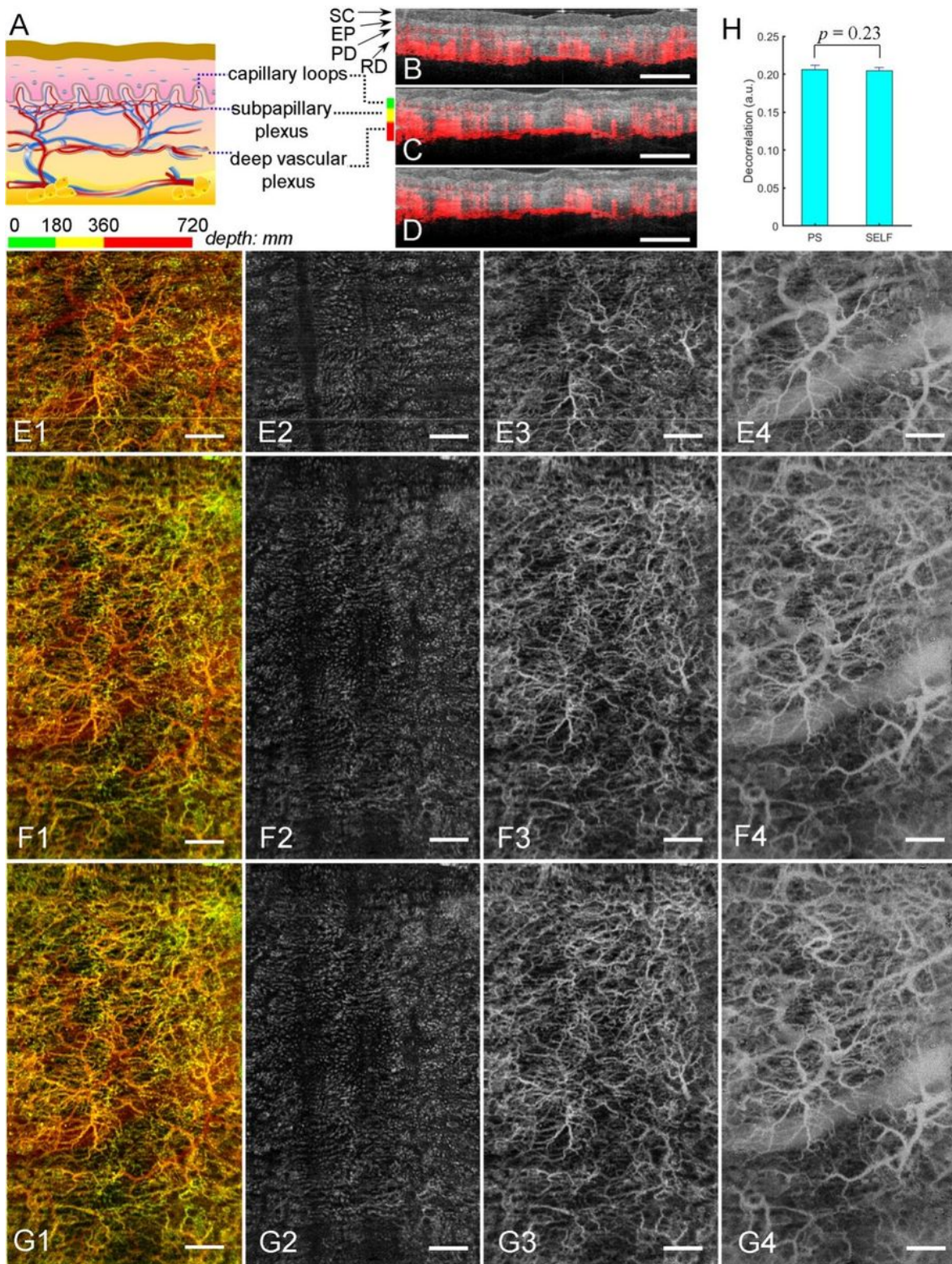


Figure 3

Comparison of FOV between the point scanning and SELF-OCTA with the same A-line rate and total acquisition time. (A) Schematic of skin structure and vasculature. **(B)** A representative OCT structural image (gray) overlaid with blood flow signals (red) acquired from the palm side of the middle finger using point-scanning scheme *in vivo*. SC: stratum corneum; EP: epidermis; PD: papillary dermis; RD: reticular dermis. **(C&D)** The corresponding images acquired with SELF scheme before (C) and after (D) Y-

deconvolution. The color bars in green, yellow and red represent the depth range of three skin slabs. (E) *En face* OCTA images acquired with the point-scanning scheme: E1, *En face* projection of skin slabs color coded by depth, E2, the first slab mainly showing capillary loops, E3, the second slab mainly containing subpapillary plexus, E4, the third slab with deep vascular plexus. (F&G) *En face* SELF-OCTA images acquired at the same region corresponding to E1-E4 before (F1-4) and after (G1-4) Y-deconvolution. (H). Decorrelation is not statistically different between the point-scanning (PS) and SELF-OCTA images. Scale bars: 1 mm.

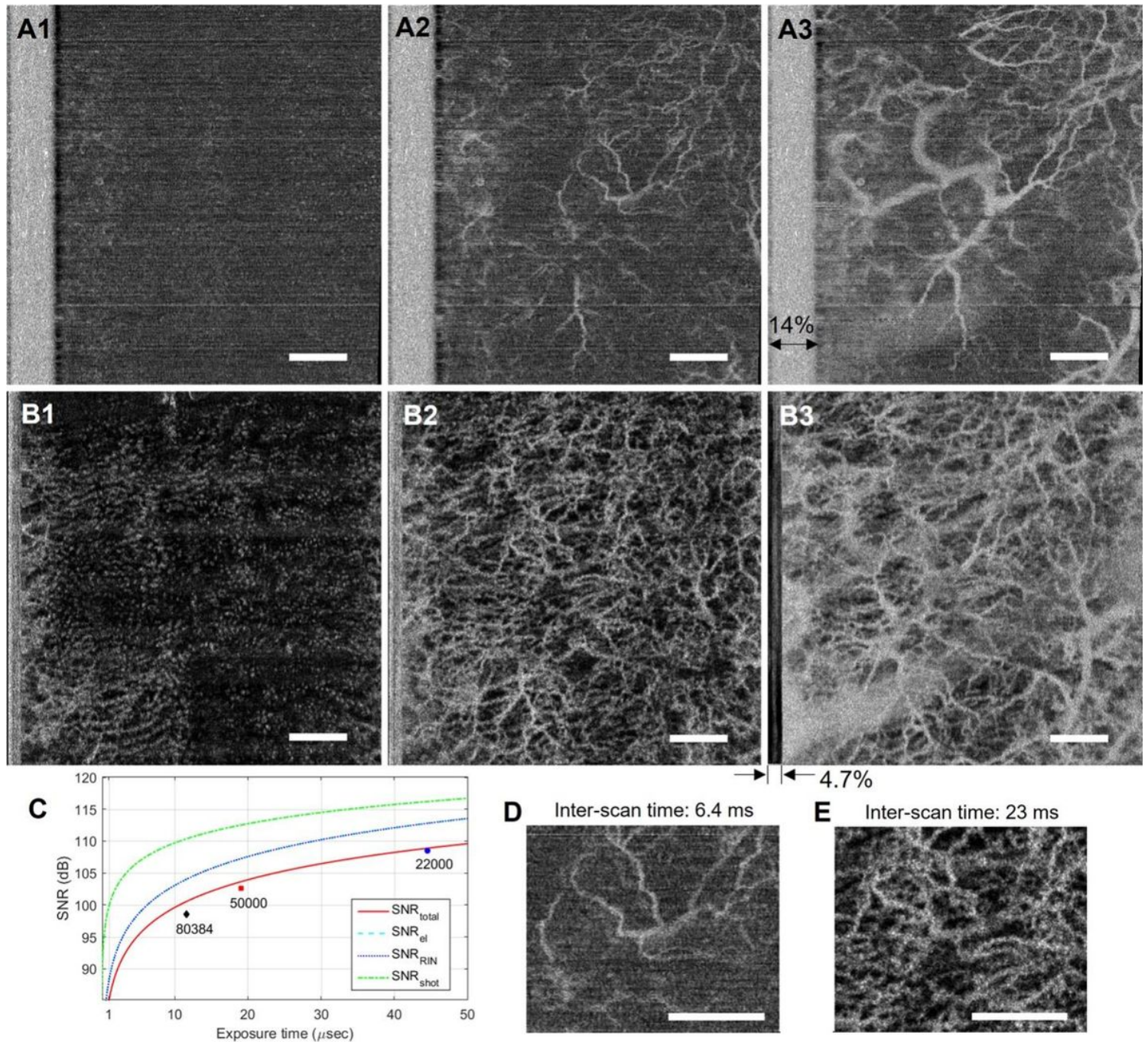


Figure 4

Comparison of vessel visibility and noise level between the point scanning and SELF-OCTA with the same input power and total acquisition time. (A1-3) *En face* OCTA projection of skin slab at the depth of capillary loop (A1), subpapillary plexus (A2) and deep vascular plexus (A3) acquired with the point-scanning scheme running at 80,384 Hz A-line rates. **(B1-3)** The corresponding SELF-OCTA images with $L = 4$ acquired at 22,000 Hz A-line rates. **(C)** Signal to noise ratio (SNR) as a function of exposure time. SNR_{el} : ratio of signal to electrical noise, SNR_{RIN} : relative intensity noise, SNR_{shot} : shot noise. Note that $SNR_{el} = SNR_{RIN}$ for optimal total SNR. Blue dot, red square and black diamond indicate measured SNR values, respectively. **(D&E)** Magnified views of a region of interest in A2 and B2. Scale bars: 1 mm.

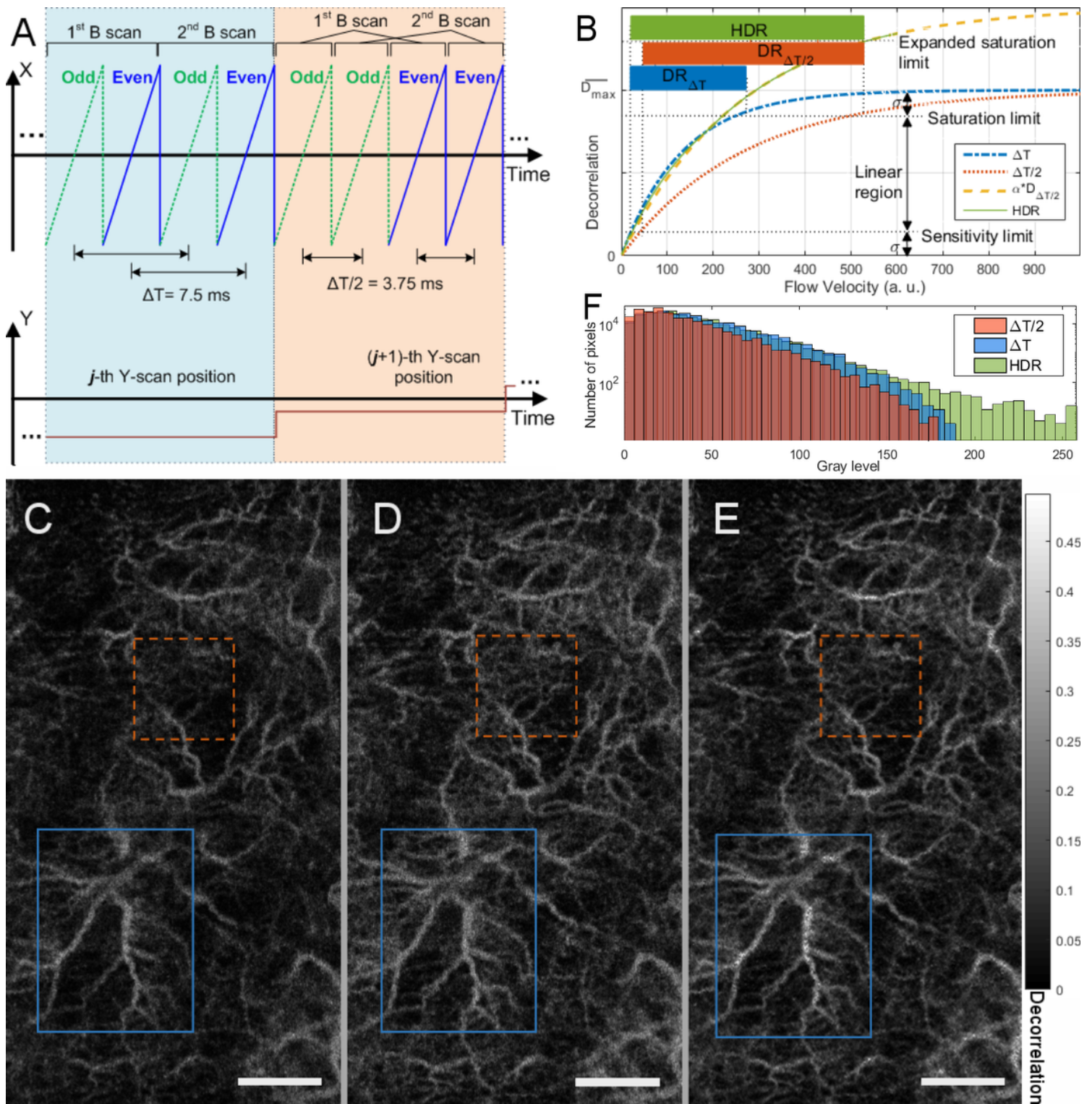


Figure 5

Multiple inter-scan time and high dynamic range (HDR). (A) Waveforms of X-Y galvanometer scanner of two consecutive Y-scan cycles. Green dashed lines stand for odd points in a B-scan, and blue solid lines represent even points in a B-scan. (B) Model of decorrelation as a function of flow velocity with different inter-scan time. σ is the mean saturated decorrelation signals, σ is the standard deviation of saturated decorrelation signals. $DR_{\Delta T}$ and $DR_{\Delta T/2}$ are the dynamic range of images acquired with inter-scan time of

ΔT and $\Delta T/2$. $D_{\Delta T}$ and $D_{\Delta T/2}$ refer to the decorrelation profiles of inter-scan time of ΔT and $\Delta T/2$, respectively. α is the ratio between decorrelation signals acquired with ΔT ($D_{\Delta T}$) and $\Delta T/2$ ($D_{\Delta T/2}$). **(C-E)** Representative *en face* angiograms acquired with $\Delta T/2$ (C) and ΔT (D), and corresponding high dynamic range reconstruction obtained according to the model in B (E). Regions marked by orange dash-line boxes show vessels appearing silent with the $\Delta T/2$ inter-scan time (C) but becoming visible with the ΔT inter-scan time (D). Regions marked by blue boxes show vessels having decorrelation signal differentiable with the $\Delta T/2$ inter-scan time (C) but undifferentiable with the ΔT inter-scan time (D). **(F)** Histograms of image grey level acquired from C, D, and E. Scale bars: 1 mm.

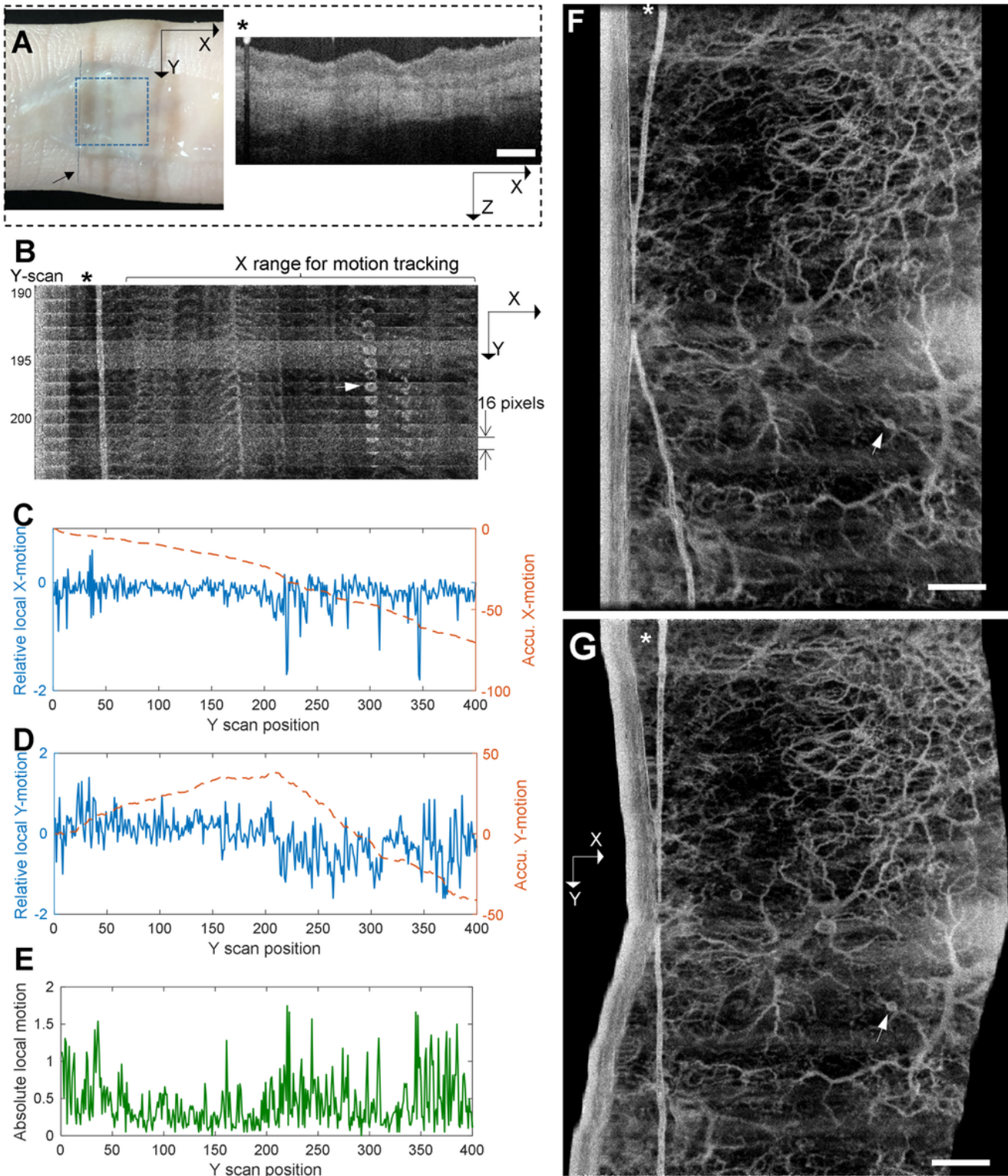


Figure 6

Motion tracking and correction based on OCTA data. (A) (left) a photograph of the proximal interphalangeal joint of the middle finger (palm side) of a healthy human subject with a segment of piano wire (arrow) attached to skin surface covered by ultrasound transmission gel. Blue dashed box indicates imaging FOV. (right) A cross-sectional OCT structural image showing the shadow of the piano wire (asterisk). (B) *En face* projections of 15 consecutive 3D angiograms with each acquired during a Y-scan

cycle. The asterisk indicates the position of piano wire. Images of an air bubble (arrow) in the gel demonstrate that the projects are overlapped. (C&D) Relative local (solid curve) and accumulative (accu.) motion (dashed curve) in X and Y-axis, respectively. The vertical unit is pixels. (E) Absolution local motion calculated as square root of sum of relative local motions squared. (F&G) A representative *en face* angiogram before (F) and after (G) motion correction, respectively. Arrows indicate the same air bubble as in B. Asterisks indicate the position of piano wire. Scale bars: 1 mm.

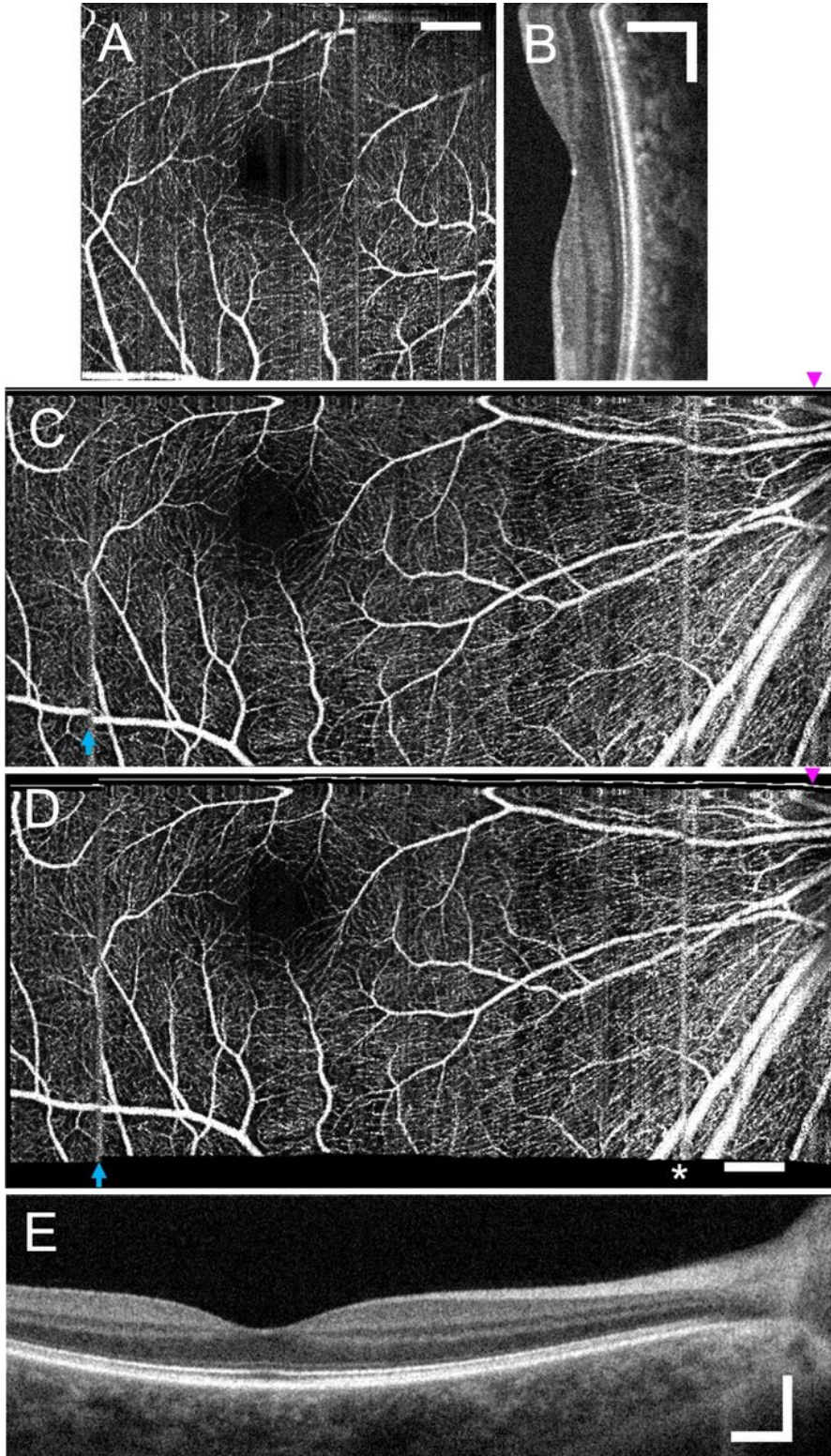


Figure 7

Retinal microvasculature. (A&B) An OCT angiogram of human inner retina (OD) using the point-scanning scheme (A), and the corresponding OCT structural image (B). (C-E) the OCT angiogram acquired with SELF scanning scheme covering both the macula and the temporal side of optic disc before (C) & after (D) motion correction, and the corresponding OCT structural image (E). A straight white line is added at the top of the uncorrected imaging, which reflects the vertical motion trajectory in the corrected image (arrowheads, C&D). Arrows indicate correction of vessel disruption. Asterisk indicates an uncorrected vessel disruption. Scale bars: 500 μm .

Supplementary Files

This is a list of supplementary files associated with this preprint. Click to download.

- [Supplementarymovie1.avi](#)
- [Supplementaryinformation.docx](#)